Eng. Sci., 2023, **24**, 896

Engineered Science
DOI: https://dx.doi.org/10.30919/es896

# Metal Ion ($Cr^{3+}$, $Eu^{3+}$, $UO_2^{2+}$) Adsorption on Gibbsite Nanoplates

Hailin Zhang,[1] Zheming Wang,[1,*] Yatong Zhao,[1] Wenwen Cui,[1] Xin Zhang,[1] Suyun Wang,[1] Eric D. Walter[2] Michel Sassi,[1] Carolyn I. Pearce,[3] Sue B. Clark[4] and Kevin M. Rosso[1]

## Abstract

Gibbsite is a common and important aluminum hydroxide mineral in natural environments and various industries, but the mechanisms by which metal ions sorb on the gibbsite surface, and their impact on surface reactivity, is not well understood. Here we examined $Cr^{3+}$, $Eu^{3+}$ and $UO_2^{2+}$ cation sorption on synthetic nanoplatelet gibbsite using vibrational sum frequency generation (VSFG) spectroscopy along with time-resolved laser-induced fluorescence spectroscopy (TRLFS), Raman/Fourier Transform Infrared (FTIR) spectroscopy, and electron microscopy. Batch sorption experiments show uptake across a broad pH range. VSFG spectra reveal cation-specific participation of surface OH groups in metal binding. For $Cr^{3+}$, uniform loss of spectral intensity with increasing cation loading indicates equal involvement of the six distinct hydroxyls. But sorption of $Eu^{3+}$ and $UO_2^{2+}$ alters its spectral profile where the reduction of the intra-layer OH bands was more pronounced and the correlation between the spectral reduction and metal ion concentration is weaker, indicating a different sorption mechanism. The latter was confirmed by the results of TRLFS analysis of both $Eu^{3+}$ and $UO_2^{2+}$ adsorbed on gibbsite.

*Keywords:* Gibbsite, Sorption, Sum frequency generation; Chromium; Europium; Uranyl.
Received: 29 April 2023; Revised: 15 May 2023; Accepted: 18 May 2023.
Article type: Research article.

## 1. Introduction

Aluminum (oxy)hydroxides, such as gibbsite ($\alpha$-$Al(OH)_3$) and boehmite (AlOOH), are major mineral components of bauxite aluminum ore, and are important secondary minerals in soils and sediments as a result of mineral weathering.[1-5] Not only are they important precursors to alumina synthesis,[6,7] but the structural and chemical characteristics of alumina surfaces in hydrous environments have been likened to that of these materials.[8,9] Understanding the surface chemistry of aluminum (oxy)hydroxides, particularly how they interact with various metals and ions in multicomponent aqueous solutions, provides insight generalizable to other related materials.[10-16]

At the atomic scale, the surfaces of the $Al(OH)_3$ polymorphs (*e.g.*, gibbsite, bayerite, and norstrandite) as well as boehmite have qualitative chemical similarities.[17-22] Their structures are based on stacked layers $Al(O,OH)_6$ octahedra polymerized by edge and corner-sharing into sheets that are held together by interlayer hydrogen bonding. The chemical behavior of stable low-index terminations of these structures is based on the details of their terminal hydroxyl groups; dominant basal surfaces tend to exhibit relatively unreactive bridging μ-hydroxyl groups whereas edge surfaces tend to exhibit more reactive singly and triply coordinated hydroxyls.[23] Because of the amphoteric nature of these surface sites, solution pH is an important master variable determining the reactivity of different crystallographic terminations.[24,25]

Unlike for acidic conditions, the effect of metal adsorption on the surface chemical behavior of these materials when exposed to highly alkaline solutions is poorly understood. This is important for production of the world's supply of aluminum through the Bayer process, and for processing of complex radioactive wastes from plutonium production at Department of Energy legacy sites, where aluminum was used as the fuel rod casing and co-disposed in large amounts with plutonium processing wastes and sodium hydroxide.[26-28] Poorly understood nucleation, growth, aggregation, and dissolution of gibbsite and boehmite particles under these conditions is a risk driver for process engineering, and questions persist about

---

[1] *Physical Sciences Division, Pacific Northwest National Laboratory, Richland, WA 99352, United States.*
[2] *Environmental Molecular Sciences Laboratory, Pacific Northwest National Laboratory, Richland, WA 99352, United States.*
[3] *Energy and Environmental Division, Pacific Northwest National Laboratory, Richland, WA 99352, United States.*
[4] *Savannah River National Laboratory, Aiken, SC 29808, United States.*
**Email:* zheming.wang@pnnl.gov (Z. Wang)

the possible influence of other metals in the waste.[26,29,30] In addition to being solid constituents of caustic nuclear wastes, gibbsite and boehmite may also encounter complex multicomponent alkaline solutions as components of host rock or engineered buffer materials in nuclear waste repositories.[31-33]

At the macroscopic scale a great deal of work has been done to understand metal ion adsorption on gibbsite and boehmite as a function of pH.[9,15,29,34-36] Using gibbsite as the example, batch sorption results show that lanthanide and actinide metal sorption strongly depends on pH and ion valence, in addition to the extent of metal ion loading which influences sorption site saturation. For trivalent ions, such as $Eu^{3+}$, $Gd^{3+}$ and $Cm^{3+}$, sorption increases slowly as the suspension pH increases from 3 to 6 and then sharply from pH 6 to ~ 7 and remains near complete coverage until pH 11. Neptunyl ($NpO_2^+$) sorption gradually increases from pH 6 to 11 reaching an ~80% maximum when concentrations range from $10^{-9}$ to $10^{-6}$ M under ambient conditions.[9,15,34] For sorption of uranyl ($UO_2^{2+}$), at ambient conditions the pH dependence is more complicated. $UO_2^{2+}$ sorption increases from pH 3 to ~ 5.5, plateaus from pH ~ 5.5 to ~ 8, and then decreases sharply due to the formation of strong negatively charged uranyl carbonate complexes that are electrostatically repelled from the surface.[37,38] The latter effect was shown to be circumvented by eliminating contact with ambient atmosphere.[39]

A molecular level understanding is required to link metal uptake observations to interactions with specific terminal hydroxyl groups. Results from time-resolved laser-induced fluorescence spectroscopy (TRLFS) on aqueous suspensions of gibbsite suggested that trivalent lanthanides and actinides can form multiple inner-sphere surface complexes involving both surface OH groups and aqueous OH ligands.[9,15] For example, multiple uranyl surface complexes form on gibbsite: two inner-sphere bidentate complexes along with uranyl hydroxide oligomers or clusters as well as possibly electrostatically bound uranyl tri-hydroxide surface complexes based on conclusions from studies using TRLFS, U-$L_{III}$ edge extended X-ray absorption fine structure (EXAFS) spectroscopy and density functional theory (DFT) calculations.[40-43] The observations suggest that metal adsorbate behavior is closely tied to specific interactions with surface hydroxyl sites, but this is inferred from the metal speciation, as these experiments do not directly probe the surface hydroxyl groups.

In this work, we examine the adsorption of $Cr^{3+}$, $Eu^{3+}$ and $UO_2^{2+}$ cations on gibbsite nanoplatelets using vibrational sum frequency generation (VSFG) spectroscopy, complemented with Raman and Fourier transform infrared (FTIR) spectroscopy, electron microscopy, and TRLFS (for fluorescing metals $Eu^{3+}$ and $UO_2^{2+}$) under basic solution conditions similar to that in the nuclear waste tanks. As a second-order nonlinear optical technique, VSFG spectroscopy is sensitive to the surface hydroxyl groups and adsorbed water where the centrosymmetry of the bulk solids and bulk solution is broken.[44-47] To our knowledge, this is the first time VSFG has been used to study metal ion sorption on minerals.

While we recently showed that $Cr^{3+}$ adsorption onto basal surfaces of boehmite nanoplates under alkaline conditions goes beyond simply adsorbed monomers, and includes polynuclear chromium hydroxide clusters, it is not known how this behavior relates to the topology of exposed hydroxyl groups.[36] Hence one of the objectives of this work is to exploit the sensitivity of VSFG to the vibrational properties of surface hydroxyl groups and how they change during $Cr^{3+}$ adsorption. Comparisons are made with $Eu^{3+}$ and $UO_2^{2+}$ adsorption to unravel the role of cation hydration characteristics on the adsorption mechanism.

## 2. Materials and methods

### 2.1 Chemicals and materials

Aluminum nitrate ($Al(NO_3)_3·9H_2O$) (≥ 98%, Sigma-Aldrich), chromium nitrate ($Cr(NO_3)_3·9H_2O$, ≥ 99%) and sodium hydroxide (NaOH) (≥ 98%) and nitric acid (ACS reagent, 70%) were purchased from Sigma-Aldrich Chemical Co. Ltd., USA. Europium chloride hexahydrate ($EuCl_3·6H_2O$, 99.99%, reagent grade) were purchased from Aldrich. An acidic uranyl stock solution was prepared by dissolving uranyl nitrate hexahydrate solid ($UO_2(NO_3)_2·6H_2O$, ACS reagent grade, 98-102%, Fisher Scientific) in 0.01 mol/L nitric acid. Dilute $HNO_3$ solution (0.01 M) was prepared by dilution of concentrated $HNO_3$. NaOH solutions (0.1 M – 3.0 M) were prepared by dissolving weighed amounts of the reagent in DDI water. Distilled and de-ionized (DDI) water was used throughout the experiments. Suspension pH was measured on a Fisher Scientific XL20 pH meter with Orion Ross Ultra semi-micro electrode that was calibrated with Fisher standard pH solutions.

### 2.2 Synthesis of gibbsite

The procedures for hydrothermal syntheses of platelet gibbsite nanoparticles has been reported previously.[48,49] Briefly, 0.25 M $Al(NO_3)_3·9H_2O$ aqueous solution was titrated with 1 M NaOH until the solution pH reached ~ 5.0. After stirring for an additional hour, the suspension was centrifuged to separate the solids. The solids were rinsed with DDI water three times and then dispersed into DDI water to $[Al^{3+}]$ ~ 0.5 M. The resulting suspension was placed in a 23 mL Teflon liner that was sealed within a Parr bomb reactor and heated in an electric oven with rotating platform (speed of 10 rpm) at 80 °C for 72 h. The resulting white solid was separated by centrifugation, washed with deionized water three times, and then dried at 80 °C overnight. Nitrogen adsorption-desorption isotherm was collected by a surface area and porosity analyzer (Micromeritics, ASAP 2020), and the Brunauer-Emmett-Teller (BET) surface areas were calculated from the linear part of the BET plot. X-ray diffraction (XRD) patterns of the samples in the 2θ range of 5−80° were recorded on a Philips X'pert Multi-Purpose Diffractometer (PANAlytical, Almelo, The Netherlands) equipped with a fixed Cu anode operating at 50 kV and 40 mA. Phase identification was done using JADE 9.5.1 from Materials Data Inc., and the 2012 PDF4+ database from the International Center for Diffraction Data (ICDD) database. The morphological imaging was performed on a Helios NanoLab 600i scanning electron microscopy (SEM, FEI, Hillsboro, OR) after sputter-coating the samples with a thin layer (~ 5 nm) of carbon prior to analysis to ensure good electron conductivity.

### 2.3 Metal ion ($Cr^{3+}$, $Eu^{3+}$ and $UO_2^{2+}$) adsorption experiments

For $Cr^{3+}$, $Eu^{3+}$ and $UO_2^{2+}$ adsorbed on gibbsite, calculated volumes of chromium nitrate, europium chloride or uranyl nitrate solutions were added to gibbsite suspensions (1 g/L) at the desired NaOH concentration, and the pH was adjusted with dilute NaOH and/or $HNO_3$. The concentration of $Cr^{3+}$ was 0.003% and 0.01% of the concentration of $Al^{3+}$ in the 1g/L gibbsite suspension, corresponding to $2.0 \times 10^{-5}$ M and $6.6 \times 10^{-5}$ M respectively, at pH 13. The $Eu^{3+}$ concentration was 0.01%, 0.1% and 1% of the concentration of $Al^{3+}$ in the 1g/L gibbsite suspension, corresponding to $2.3 \times 10^{-5}$ M, $2.3 \times 10^{-4}$ M and $2.3 \times 10^{-3}$ M respectively, each at pH 5, pH 13 and 3 M NaOH. The $UO_2^{2+}$ concentration was 0.001%, 0.01% and 0.1% of the total $Al^{3+}$, corresponding to $1.5 \times 10^{-6}$ M, $1.5 \times 10^{-5}$ M and $1.4 \times 10^{-4}$ M respectively, both at pH 5 and pH 13. The solid suspensions were then slowly shaken on an orbital shaker for 24 h, followed by phase separation via centrifugation at 2000 rcf for 30 min. The resulting solid pastes were dried at 80 °C for 24 h and then subjected to spectroscopic analysis. Selected supernatant liquids were acidified to verify the amounts of metal ion adsorption via inductively-coupled plasma – optical emission spectrometry (ICP-OES) (Perkin Elmer Optima 2100 DV, with calibration standards from Ultra Scientific, Inc., Kingstown, RI, and Inorganic Ventures, Inc., Christiansburg, VA). To prevent the contamination of atmospheric $CO_2$, all experiments were conducted in a dry $N_2$ atmosphere glove box. Samples for fluorescence analysis were transferred into 2 mm × 4 mm × 25 mm quartz cuvettes, tightly capped with silicone stoppers, and sealed with parafilm prior to removal from the $N_2$ atmosphere chamber.

### 2.4 Spectroscopic analyses

For VSFG spectroscopy analysis, we used a picosecond scanning VSFG system as described previously.[50-52] Briefly, the VSFG spectrometer consists of a customized commercial EKSPLA laser system (EKSPLA PL2251A-50) running at 10 Hz, with a pulse width of 29 ps. A part of the fundamental Nd:YAG laser output (1064 nm) was frequency-doubled to 532 nm using a KD*P crystal and the rest is used to pump an optical parametric generation/amplification and difference frequency generation system (EKSPLA PG401/DFG) to produce an IR beam tunable from 650 $cm^{-1}$ to 4300 $cm^{-1}$. The fixed 532 nm beam and tunable infrared (IR) beam were focused on the sample surface with an incident angle of 65° (visible) and 55° (IR), respectively, to overlap spatially and temporally to generate the sum-frequency signal, which passes through a polarizer and is then dispersed through an Andor Shamrock M spectrometer and detected by a Hamamatsu R585 photomultiplier tube (PMT). The signal was collected and plotted after normalization to the laser energies and gains of the PMT, while scanning the frequency of the IR beam between 3800 $cm^{-1}$ to 3200 $cm^{-1}$. The pulse energy of the visible beam was maintained at around 110 μJ, while the pulse energy of the IR beam applied was around 80 μJ. The VSFG spectrometer offers an overall spectral resolution of approximately 6 $cm^{-1}$.

The TRLFS spectra of $Eu^{3+}$-/$UO_2^{2+}$-adsorbed gibbsite samples were obtained using a Nd:YAG laser (Spectra-Physics Quanta-Ray PRO) pumped MOPO laser (Lasertechnik-GWU) equipped with a FDO-900 scanning frequency doubler, running at 10 Hz (pulse width ∼40 ns) by excitation at 394 nm for $Eu^{3+}$ and 415 nm for $UO_2^{2}$.[53,54] For $UO_2^{2+}$-adsorbed gibbsite samples, the luminescence measurement was performed at near liquid helium temperature.[53,54] The resulting fluorescence was collected at ~85° in respect to the excitation beam by a 2 inch diameter f/3 fused silica lens, focused by a 2 inch f/4 fused silica lens into the entrance slit of a 0.3 m focal length Acton SpectroPro 300i double monochromator spectrograph and recorded by a thermoelectrically cooled Princeton Instruments PIMAX time-gated intensified CCD camera that was triggered by the delayed output of the laser pulse and controlled by the WinSpec™ Data acquisition software. Fluorescence decay curves of the $Eu^{3+}$-/$UO_2^{2+}$-adsorbed samples were obtained by sequentially recording fluorescence spectra at different delay times and then plotting the spectral intensity as a function of the delay time. The emission spectra and decay data were analyzed using commercial software, IGOR®, from Wavematrix, Inc.

Raman spectra were recorded using a Horiba LabRam HR spectrometer coupled with an inverted optical microscope (Nikon Ti-E) and a 632.8 nm HeNe laser light source. Spectra were collected with a 40X objective in backscattered geometry in the spectral range of 150−4000 $cm^{-1}$ range. The collected Raman signal was transmitted through a beamsplitter, dispersed through an 1800 g/mm grating and detected by an EM-CCD detector. ATR-FTIR spectra were measured using a Bruker Alpha II Fourier transform infrared spectrometer (FTIR) spectrometer. The presented FTIR spectrum were the average of the average of five consecutive measurements, each consisted of 128 scans at a resolution of 4 $cm^{-1}$.

## 3. Results and discussion

### 3.1 Structural characterization of synthetic gibbsite

The XRD pattern for the as-synthesized gibbsite was consistent with the reference pattern for gibbsite in the ICDD database (ICDD PDF # 00-33-0018) (Fig. 1 and SI Fig. 1).[49,55] SEM images show that the gibbsite particles have a uniform hexagonal platelet morphology, with a diameter of ~ 500 nm

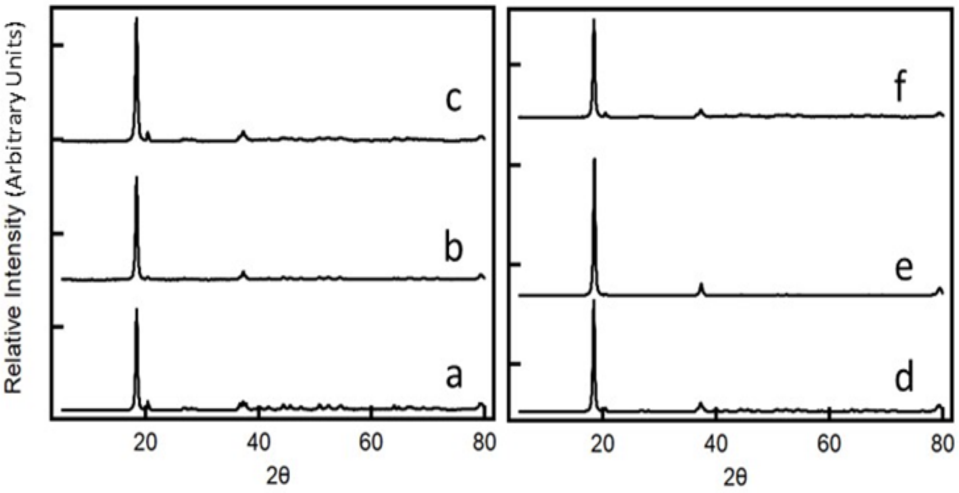

**Fig. 1** XRD patterns of as-synthesized gibbsite (a), U-adsorbed gibbsite, pH 5 (b), U-adsorbed gibbsite, pH 13 (c), Eu-adsorbed gibbsite (d, e, f) at pH 5, 13 and 3 M NaOH. The concentration of added U or Eu were all at 0.1% relative to Al concentration. For clarity, the XRD traces were arbitrarily re-scaled and offset along the y-axis.

and a thickness of ~ 10 – 20 nm (Fig. 2 and SI Fig. 2). The measured BET surface area was 52.2 $m^2/g$, which is similar to published data for gibbsite synthesized using the same method.[56,57] Raman spectra showed four discrete peaks in the OH stretch frequency range at 3623, 3527, 3435 and 3364 $cm^{-1}$, respectively (Fig. 3). Similarly, four IR bands, though less resolved, were also present in the ATR-FTIR spectra in the same region as the broad OH stretch band of hydration waters (Fig. 4).

The features in the Raman spectra correspond to specific OH groups in the bulk gibbsite crystal structure. In this structure, $Al^{3+}$ cations occupy 2/3 of the octahedral cavities between pseudo-hexagonally close-packed hydroxyl groups stacked along the z-direction with hydroxyls in each layer pointed in the opposite directions to those in adjacent layers (Fig. 5).[49, 57-60] There are a total of six structurally distinct OH groups within each unit layer, three in intra-layer directions and three in the inter-layer direction, which has been confirmed with polarized Raman and IR spectroscopy analysis under cryogenic conditions.[59] At room temperature, only four bands are commonly observed due to spectral broadening that causes band overlap, consistent with our observations.[49,57]

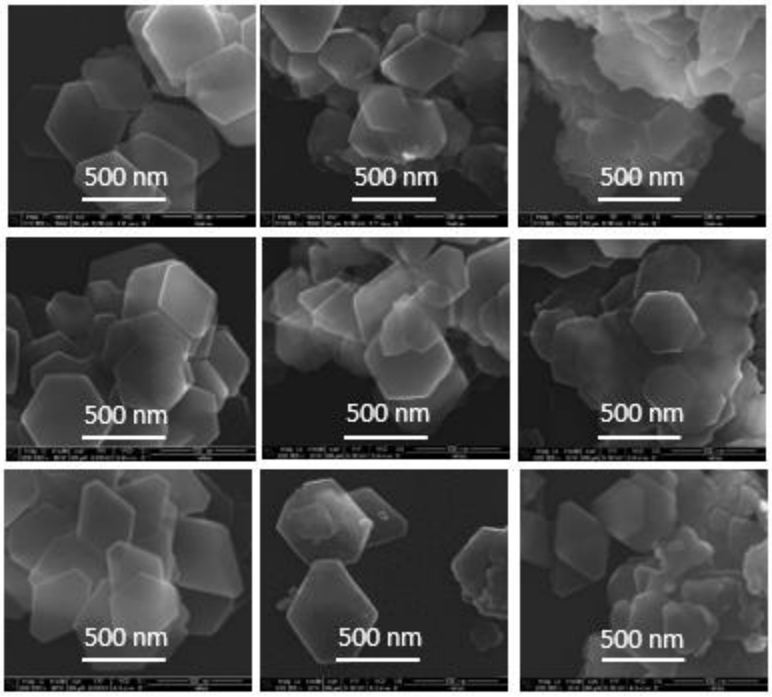

**Fig. 2** SEM images of Eu-adsorbed at gibbsite with 0.01% Eu (top row), 0.1% Eu (middle row), 1%Eu (bottom row) at pH 5 (left column). pH 13 (middle column) and in 3.0 M NaOH (right column).

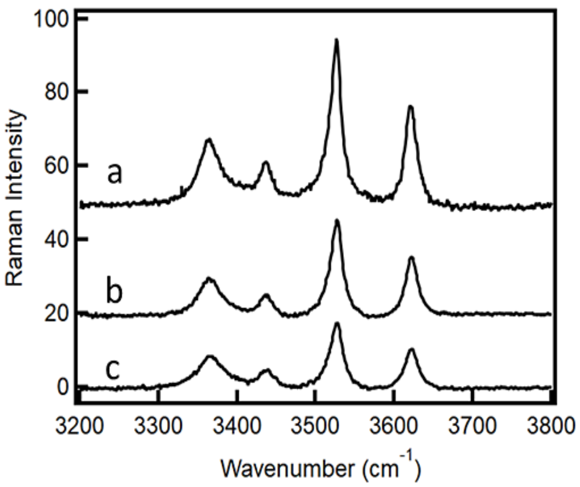

**Fig. 3** Raman spectra of the synthesized gibbsite (a), Cr-adsorbed gibbsite at [Cr] = 0.003% (b) and Cr-adsorbed gibbsite at [Cr] = 0.01% (c).

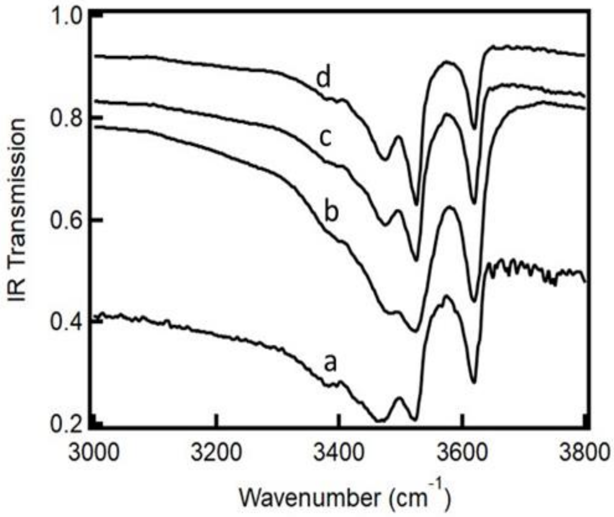

**Fig. 4** IR spectra of the synthesized gibbsite (a), Eu-adsorbed gibbsite at Eu 1% in 3M NaOH (b), Eu-adsorbed gibbsite at Eu 0.01%, pH 5 (c) and Eu-adsorbed gibbsite at Eu.

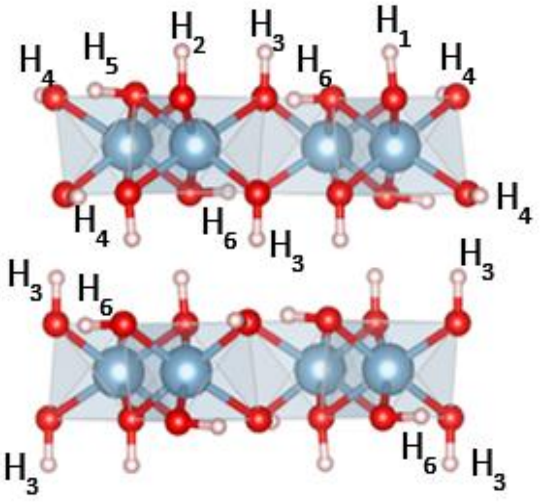

**Fig. 5** The crystal structure of gibbsite showing the six unique hydroxyl groups.

### 3.2 Impact of metal ion adsorption on bulk gibbsite characteristics

All three metal ions ($Cr^{3+}$, $Eu^{3+}$ and $UO_2^{2+}$) adsorb on gibbsite with the amount depending on the suspension pH, metal ion concentration and the mass loading ratio of gibbsite to the metal ion in solution (Table 1, SI Table 1). After separation of the solids from the solution by centrifugation, measurement of the remaining metal ion concentration in the supernatants showed that for $Eu^{3+}$, uptake was less than 13% at pH 5 but reached 88% to nearly 100% at pH 13 and in 3 M NaOH, respectively (Table 1). For $UO_2^{2+}$ adsorption, its uptake varied between 82% to 94% and its relative adsorption was higher at pH 13 than at pH 5 and increased as the initial $UO_2^{2+}$ concentration decreased (SI Table 1). The higher relative $UO_2^{2+}$ adsorption as compared with those reported by Baumann *et al*.[43] was likely due to the much higher surface area of the gibbsite nanoparticles in this work (52.2 m$^2$/g vs. 1.5 m$^2$/g) as well as the absence of $CO_2$ which suppressed the formation of highly stable uranyl tricarbonate complexes typical in basic solutions.[61] For $Cr^{3+}$, the uptake was 23% and 12% at initial $Cr^{3+}$ solution concentrations of 0.003% and 0.01%, respectively.

**Table 1**. ICP-MS results for Eu(III) in solution before (initial) and after (final) adsorption on gibbsite at 25 °C.

| Sample Conditions | $[Eu(III)]_{Initial}$ (mM) | $[Eu(III)]_{Final}$ (mM) | $Eu(III)_{Adsorbed}$(%) |
|---|---|---|---|
| 1% Eu – 3 M NaOH | 0.128 | 0.029 | 97.7 |
| 1% Eu – pH 13 | 0.128 | 0.00008 | 99.9 |
| 1% Eu – pH 5 | 0.128 | 0.124 | 3.31 |
| 0.1% Eu – 3 M NaOH | 0.0128 | 0.0085 | 93.3 |
| 00.1% Eu – 3 M NaOH | 0.0128 | 0.0001 | 99.2 |
| 0.1% Eu – pH 5 | 0.0128 | 0.0011 | 12.8 |
| 0.01% Eu – 3 M NaOH | 0.00128 | 0.0015 | 88.5 |
| 0.01% Eu – pH 13 | 0.00128 | 0.0001 | 97.7 |
| 0.01% Eu – pH 5 | 0.00128 | ---* | ---* |

* Not measured.

SEM revealed no significant change in particle size or shape for the metal-adsorbed gibbsite, except in the 3.0 M NaOH solutions, in which dissolution of the gibbsite resulted in particles with more rounded edges (Fig. 2, right column).

The Raman spectra were recorded for both $Cr^{3+}$- and $Eu^{3+}$-adsorbed gibbsite samples (Fig. 3 traces b and c, SI Fig. 3). As seen in Fig. 3, $Cr^{3+}$ adsorption leads to lowered Raman spectral intensity for all four bands and the magnitude of intensity reduction increased as the concentration of added $Cr^{3+}$ increased from 0.003% to 0.01%, yet the spectral positions remained unchanged. Although the Raman signal is a bulk measurement, this loss of spectral intensity in the OH region is a clear indication that Cr adsorption occurred through interaction with hydroxyl groups, likely the fraction exposed at the surface. For the thin nanoplatelets, the surface hydroxyls contribute nearly 30% of the total hydroxyl content as estimated by the average size and particle geometry of the gibbsite nanoplatelets. Cation exchange with surface protons on these hydroxyl groups is one possible adsorption mechanism consistent with this change in the Raman spectra. The peak positions of the two sharpest and strongest bands on the high frequency end also show minor shifts due to $Cr^{3+}$ adsorption. For example, the highest frequency peak originally located at 3619.6 $cm^{-1}$, corresponding to the intra-layer hydroxyls, shifts to 3621.4 $cm^{-1}$ and 3623.3 $cm^{-1}$after gibbsite exposure to 0.003% and 0.01% $Cr^{3+}$ solutions, respectively.

FTIR spectra were recorded for $Eu^{3+}$-adsorbed gibbsite samples. Similar to the Raman spectral behavior, four bands were observed in the FTIR spectra for the as-synthesized gibbsite as well as $Eu^{3+}$ adsorbed gibbsites at all three initial $Eu^{3+}$ concentrations, and there is no noticeable differences in the spectral band maxima (Fig. 4).

### 3.3 Interfacial vibrational spectroscopic analyses

VSFG spectroscopy allowed direct interrogation of the surface hydroxyl groups before and after metal cation adsorption without interference of the -OH groups within the bulk nanocrystal. VSFG measurements were performed using a fixed visible laser beam at 532 nm while scanning the IR laser beam across the same OH stretch frequency region observed in the Raman/FTIR (3200 - 3800 $cm^{-1}$) (Fig. 6). In VSFG, the sum frequency signal, $I_{SFG}$, can be expressed as Eq. (1):

$$I_{SFG} = \left|\chi^{(2)} \times E_{\omega\,Vis} \times E_{\omega\,IR}\right|^2 \qquad (1)$$

where $E_{\omega Vis}$ and $E_{\omega IR}$ are the visible and IR electric fields. $\chi^{(2)}$ is the second-order susceptibility of the material for SFG and is described by Eq. (2):

$$\chi^{(2)} = \chi_{NR}^{(2)} + \sum_k \frac{A_k}{\omega_k - \omega_{IR} - i\Gamma_k} \qquad (2)$$

where $\chi_{NR}^{(2)}$ is the non-resonant contribution of the material, $\omega_{IR}$ is the IR frequency; $A_k$ is the amplitude of the *k*th resonant mode with corresponding peak frequency and half width of $\omega_k$ and $\Gamma_k$, respectively. $\chi_{NR}^{(2)}$ is intrinsic to the substrate material. For common dielectric minerals such as silica and alumina, it is usually featureless and small.[45,62-64] For a given chemical system the value of $A_k$ is proportional to the concentration of the active surface species, its Raman tensor and IR transition dipole moment. As can be seen from Eq. (2), if $\chi_{NR}^{(2)}$ is constant, which is the case for gibbsite,[56] larger χ(2) values will appear at or near the IR absorption bands of the surface species when the frequency of the electric fields involved in the process overlaps with that of a transition between two vibrational levels of the material, leading to "resonance enhancement".[47,65-67]

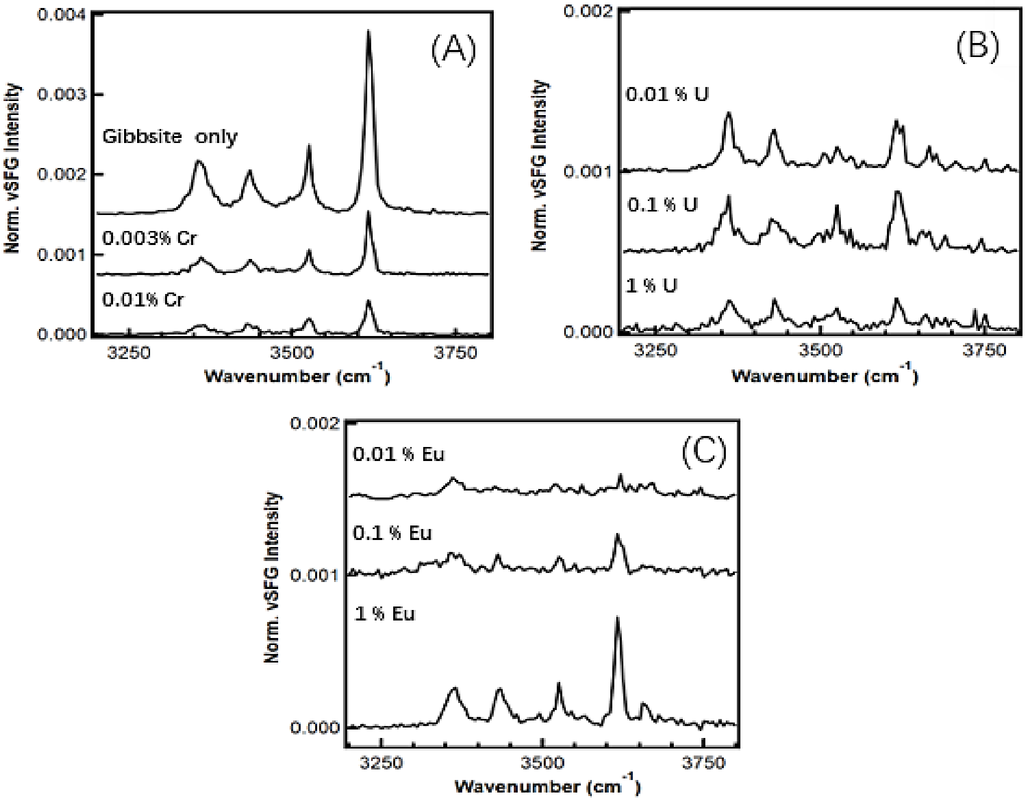

**Fig. 6** VSFG spectra of gibbsite in 0.1 M NaOH with adsorbed metal ions: $Cr^{3+}$(A); $UO_2^{2+}$ (B); and $Eu^{3+}$ (C). All metal ion concentrations are relative to [Al]. Spectral traces are off set in the Y-axis for clarity.

As shown in Fig. 6A, pristine gibbsite nanoplatelets showed strong, well-resolved VSFG spectra with band maxima located at 3615, 3525, 3425 and 3355 cm$^{-1}$, with shoulder bands at ~3500 cm$^{-1}$ and 3355 cm$^{-1}$. Once any of the three metal cations are adsorbed, the intensity of all four surface -OH bands decreased, consistent with the bulk Raman and indicating a prominent effect of adsorbed metals on surface hydroxyl groups. The relative peak intensities among the four VSFG peaks of gibbsite varied depending on the specific metal adsorbed (Fig. 6). For pristine gibbsite, the intensities of the intra-layer hydroxyl bands at 3615 and 3525 cm$^{-1}$ are higher than the inter-layer hydroxyl bands at 3425 and 3355 cm$^{-1}$, with the peak at 3615 cm$^{-1}$ about 3.7 times higher than the 3355 cm$^{-1}$ (Fig. 6A). The same trend follows for $Cr^{3+}$-adsorbed gibbsite and $Eu^{3+}$-adsorbed gibbsite (Figs. 6A and C). However, for $UO_2^{2+}$-adsorbed gibbsite, the 3615 cm$^{-1}$ band displays approximately the same intensity as those of the 3425 and 3355 cm$^{-1}$ bands and the intensity of the 3525 cm$^{-1}$ band is mostly lower than those of the 3425 and 3355 cm$^{-1}$ bands (Fig. 6B).

The present findings confirm that metal cation adsorption entails strong disruption of the surface OH configuration, likely through partial deprotonation during cation exchange to form adsorbed metal surface complexes. The peak intensities of the strongest VSFG band of gibbsite at ~ 3615 cm$^{-1}$ decreased by ~ 95% ($Eu^{3+}$ 0.01%) to 65% ($Cr^{3+}$ 0.001%), depending on the specific cation and their initial concentrations (Fig. 7). While for both $Cr^{3+}$ and $UO_2^{2+}$, the peak intensity reduction appeared to increase as the initial metal ion concentration increased, the opposite trend was observed for $Eu^{3+}$, suggesting different adsorption mechanisms for $Eu^{3+}$.

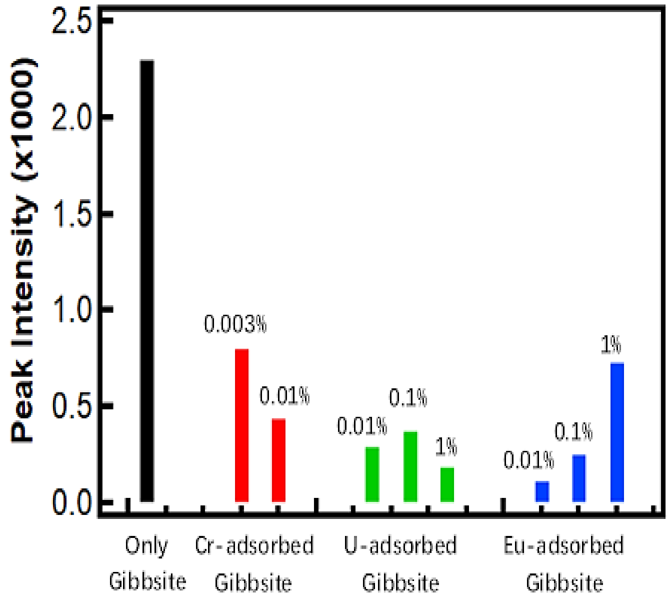

**Fig. 7** Maximum VSFG peak intensity of gibbsite with and without metal ions adsorbed at ~3615 cm$^{-1}$ in 0.1 M NaOH (the percentage values in the bar graph are the initial concentrations of the corresponding metal ions).

These observations support the hypothesis that adsorption of the three metals may not involve the same hydroxyl groups. In the case of $UO_2^{2+}$, more intra-layer hydroxyl groups appear to be involved in the formation of surface complexes, as reflected by a decrease in the band intensities. This suggests that $UO_2^{2+}$ preferentially binds to these hydroxyl orientations. This may further indicate a preference for $UO_2^{2+}$ to bind to particle edge sites, where these intra-layer hydroxyl groups are exposed. Previous electron microscopy and X-ray photoelectron spectroscopy studies of boehmite nanoplates also showed preferential binding of $Cr^{3+}$ at (101) edge surfaces,[29] which hindered subsequent dissolution by blocking the most reactive corner and edge sites, as confirmed by high-resolution transmission electron microscopy.[30] Additional support consistent with the intrinsically pivotal role played by surface hydroxyl groups during metal binding comes from the prior discovery of $Cr^{3+}$ cluster formation on boehmite surfaces, which appeared to be catalyzed, at least in part, by short-range epitaxial lattice matching between the topology of basal surface hydroxyls and that of CrOOH polymorphs.[30] The intimate association of $Cr^{3+}$ coordination clusters with the boehmite surface implies formation of Cr-O(H)-Al bridging bonds that undoubtedly entails disruption of the configuration and/or protonation state of the surface hydroxyls. Given our current observations, it seems plausible that such oligomeric surface complexes also form during adsorption of $Eu^{3+}$ and $UO_2^{2+}$ cations, with differences linked to the discrepancy between the larger ionic radii of $Eu^{3+}$ and $UO_2^{2+}$ compared to $Al^{3+}$, versus the similar ionic radii of $Cr^{3+}$ and $Al^{3+}$.

### 3.4 TRLFS characterization of $Eu^{3+}$ and $UO_2^{2+}$adsorbed on gibbsite.

Both $Eu^{3+}$ and $UO_2^{2+}$ cations display unique luminescence properties upon absorption in the UV-visible region.[68-74] Their absorption and luminescence spectral position, band splitting pattern and relative intensity are dependent on the local bonding and symmetry around the metal ion.[53,75-84] For example, ligand coordination typically leads to longer luminescence lifetimes for both $Eu^{3+}$ and $UO_2^{2+}$. In case of $Eu^{3+}$, the luminescence decay constant in aqueous solution is linearly correlated with the number of bound hydration waters or OH moieties.[70,85] Here we used nanosecond pulsed laser-induced time-resolved luminescence analysis to gain deeper insight into how $Eu^{3+}$ and $UO_2^{2+}$ adsorb on gibbsite nanoplatelets.

The TRLF spectrum for 0.1 % $Eu^{3+}$ adsorbed on gibbsite at pH 13 had well-resolved peaks at 574.5 nm, 593.1 nm, 618.0 nm, 653.5 nm, and 698.2 nm (Fig. 8). These peaks correspond to the electronic transitions $^5D_0 \rightarrow {}^7F_j$ (j = 0, 1,2,3 and 4), respectively, of the $Eu^{3+}$ cation.[76] The $^5D_0 \rightarrow {}^7F_2$ transition, which is of electric dipole character, shows a large dependence on the coordinating ligand field, but for the $^5D_0 \rightarrow {}^7F_1$ transition, which is of magnetic dipole character, the radiative transition probability is minimally influenced by the ligand

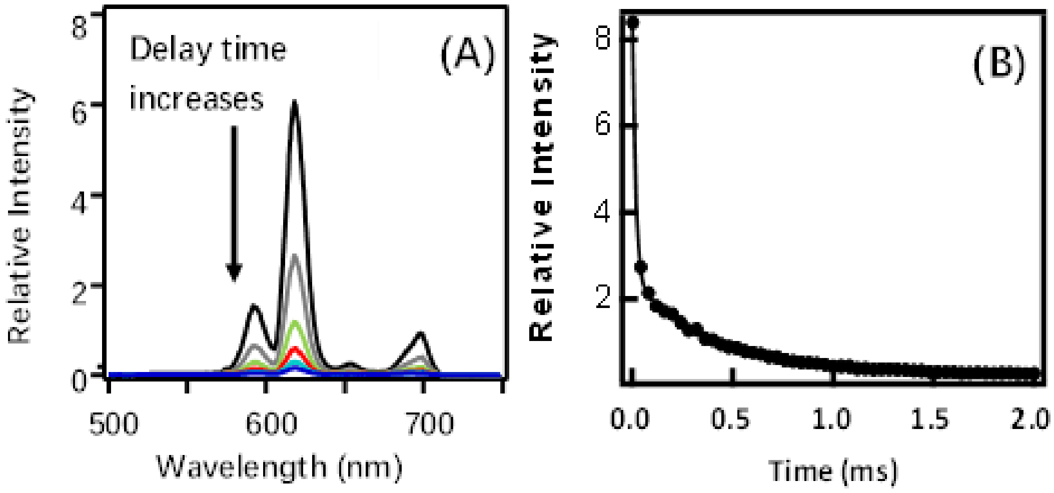

**Fig. 8** Time-resolved TRLFS spectra of Eu-adsorbed gibbsite at Eu 0.1%, pH 13 (A) and the corresponding luminescence decay trace (B) and the fitted curve (solid line).

field. Thus, the relative intensities of the $^5D_0 \rightarrow {}^7F_2$ band at ~ 614 nm and the $^5D_0 \rightarrow {}^7F_1$ band at ~ 593 nm and the spectral shift of the former can be used as an indicator of coordinating ligand field strength around Eu$^{3+}$.86 For the aqueous Eu$^{3+}$ cation (e.g., in the bulk aqueous EuCl$_3$ solution), the peak corresponding to the $^5D_0 \rightarrow {}^7F_2$ transition appears at 616 nm with a spectral intensity of ~ 25% that of the peak corresponding to the $^5D_0 \rightarrow {}^7F_1$ at ~ 593 nm.[68] In comparison, for Eu$^{3+}$ adsorbed on gibbsite, the peak position of the $^5D_0 \rightarrow {}^7F_2$ transition is red-shifted 2 nm to 618.0 nm and its spectral intensity is 3.6 times more intense than that of the $^5D_0 \rightarrow {}^7F_1$ band, indicating that the Eu$^{3+}$ ion forms strong inner-sphere surface complexes on gibbsite.

In agreement with the spectral changes, the primary component of the measured luminescence lifetimes of Eu$^{3+}$-adsorbed on gibbsite (Table 2) were much longer than that of the fully hydrated Eu$^{3+}$ ion (~ 117 μs[68,87]). Using the linear correlation between the measured luminescence decay constant and the number of hydration waters in the inner coordination sphere of the Eu$^{3+}$ ion,[85]

$$N_{H_2O} = 1.07 \cdot k_{H_2O} - 0.7 \quad (3)$$

In Eq. (3), $N_{H_2O}$ is the number of water molecules remaining in the inner coordination sphere and $k_{H_2O}$ is the measured fluorescence decay constant of the Eu$^{3+}$ (in ms$^{-1}$). For Eu$^{3+}$ adsorbed on gibbsite, the primary $N_{H_2O}$ values fall in the range from 7.2 in 3 M NaOH at 0.01% initial Eu concentration to 1.9 at pH 13 with an initial Eu concentration of 0.1% (Table 2). In aqueous solution, the Eu$^{3+}$ ion has an average inner-sphere hydration number of ~ 8.5±0.5.[87] Thus, adsorption of Eu$^{3+}$ on gibbsite via surface complexation removes 1.3-6.4 inner-sphere hydration waters, which is consistent with the observed spectral changes (Fig. 8).[76,85] This large variation in the number of inner-sphere hydration waters may indicate that there are multiple surface binding sites for Eu$^{3+}$. The presence of a minor fast luminescence decay pathway, as reflected by a lifetime (data in parenthesis of Table 2) shorter than that of the aqueous Eu$^{3+}$ ion, may indicate the presence of Eu$^{3+}$ clusters in the system.[53,88,89]

**Table 2.** Luminescence lifetimes (25 °C) and calculated hydration numbers of Eu(III) adsorption on gibbsite.

| Sample Conditions | Luminescence Lifetimes (μs) | Eu(III) Hydration Number [a] |
|---|---|---|
| 1% Eu – 3 M NaOH | 157 | 6.1 |
| 1% Eu – pH 13 | 383, (0.174) [b] | 2.1 |
| 1% Eu – pH 5 | N.M. | N.M. |
| 0.1% Eu – 3 M NaOH | 260 | 3.4 |
| 0.1% Eu – pH 13 | 408, (12) [b] | 1.9 |
| 0.1% Eu – pH 5 | 297, (32.5) [b] | 2.9 |
| 0.01% Eu – 3 M NaOH | 136, (16.1) [b] | 7.2 |
| 0.01% Eu – pH 13 | N.M. | N.M. |
| 0.01% Eu – pH 5 | 162 | 5.9 |

[a] Hydration number calculation method has an error of ± 0.5 (and the faster decay component in parenthesis is not considered). [b] Minor component with larger fitting error. N.M. = not measured.

For UO$_2^{2+}$ adsorbed on gibbsite, the liquid helium temperature (LHeT) TRLFS spectra displayed strong luminescence spectra (Fig. 9A and SI Figs. 4-6), with enhanced spectral resolution as the delay time after the laser pulse increased. Such spectral changes indicate the presence of more than one unique UO$_2^{2+}$ coordination environment.[90-92] For most samples, it was found that the spectral profiles at long delay times (≥ 1 ms) displayed minimal changes, suggesting that it likely represents a unique UO$_2^{2+}$ surface complex. By subtracting the spectral contribution of this species iteratively from the TRLFS spectra at shorter delay times, the spectra representing a shorter-lived UO$_2^{2+}$ species can be obtained. The results of such a spectral analysis for 0.1% UO$_2^{2+}$ adsorbed on gibbsite at pH 13 are shown in Fig.

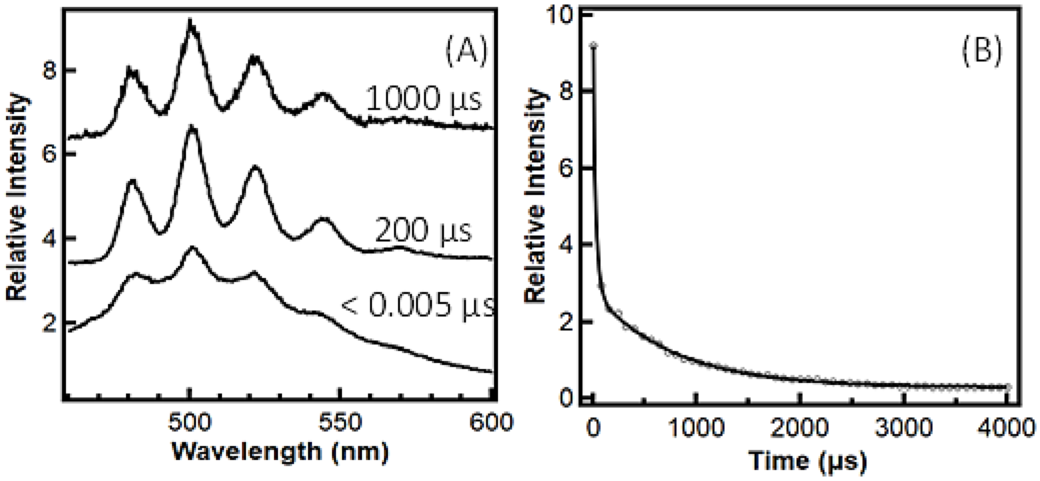

**Fig. 9** TRLFS spectra at three different delay times (A) and luminescence decay data (open circles) with biexponential fitting results (solid line) (B) of U-adsorbed gibbsite at U 0.1%, pH 13. $\lambda_{ex}$ = 415 nm.

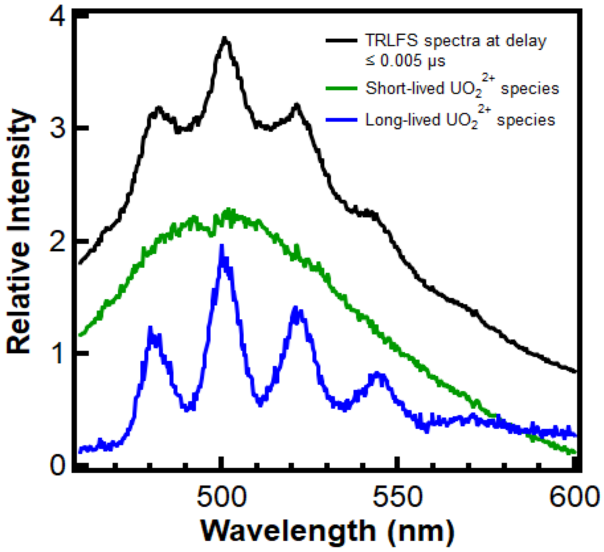

**Fig. 10** Deconvoluted TRLFS spectra at delay time ≤ 0.005 µs for U-adsorbed gibbsite at U 0.1%, pH 13.

10. While the TRLFS spectra at long delay time (1 ms) (blue spectrum in Fig. 10) representing a unique long-lived luminescent adsorbed $UO_2^{2+}$ species displayed well-resolved vibronic bands at 481.9 nm, 500.8 nm, 521.2 nm, 543.7 nm and 568.8 nm, respectively, the spectra representing a short-lived species showed poor spectral resolution and a spectral maximum at ~ 505 nm (green spectrum in Fig. 10). For the former, the average vibronic peak spacing of ~ 790.6 cm$^{-1}$ falls well within the range for uranyl oxyhydroxide species,[93] which likely reflects the nature of $UO_2^{2+}$ bonding to hydroxyl groups to form complexes on the gibbsite surface. The luminescence decay curve is best fit by a bi-exponential function (Fig. 9B) with luminescence lifetimes of 778±16 µs and 28±2 µs, respectively, consistent with the presence of two uranyl surface species, which is in agreement with the spectral analysis. The bonding and structures of the $UO_2^{2+}$ surface species are dependent on solution pH, as well as initial $UO_2^{2+}$ concentration, based on the shifts of the vibronic bands of the long-lived $UO_2^{2+}$ species. For example, at an initial $UO_2^{2+}$ concentration of 0.001%, the four vibronic bands are located at 479.9 nm, 499.7 nm, 521.7 nm and 538.5 nm, respectively at pH 5, while they shifted to 471.4 nm, 491.8 nm, 512.9 nm and 535.2 nm, respectively, at pH 13.

## 4. Conclusion

The results from batch adsorption and surface specific VSFG studies show that the sorption of metal ions $Cr^{3+}$, $Eu^{3+}$ and $UO_2^{2+}$ on gibbsite occurs across broad pH conditions from weakly acidic to highly basic conditions. VSFG spectra indicate that, within the metal ion concentration range studied (0.001% to 0.1% relative to total Al), sorption of metal ions leads to reduction of the spectral intensity of gibbsite surface OH groups, indicating participation of the surface OH in metal ion bonding, which likely occurs via metal ion substitution for the hydroxyl proton. The VSFG spectra show that the three metal ions had different sorption characteristics. For $Cr^{3+}$, the spectra for different $Cr^{3+}$ concentrations are similar to that for as-synthesized gibbsite, and the reduction of the VSFG band intensities are inversely correlated with $Cr^{3+}$ concentration. This suggests that the six distinct surface hydroxyls on the gibbsite basal surface are equally involved in $Cr^{3+}$ binding, within the concentration range studied. However, for both $Eu^{3+}$ and $UO_2^{2+}$, the spectral profile for gibbsite was altered when the metal ion was adsorbed. The reduction in intensity of the higher frequency bands corresponding to intra-layer hydroxyl groups (~ 3620 cm and ~ 3519 cm) was more pronounced, particularly in the case of $Eu^{3+}$, indicating that these hydroxyls preferentially bind $Eu^{3+}$ and $UO_2^{2+}$. Considering the much larger ionic radii of $Eu^{3+}$ and $UO_2^{2+}$ as compared to both $Cr^{3+}$ and the substrate metal ion $Al^{3+}$, this suggests that the sorption involves edge sites where intra-layer hydroxyls are more accessible. The weak correlation between the decrease in spectral intensity and metal ion concentration also suggests that surface metal ion adsorption involves metal oxide clusters. The redshift of the luminescence spectra of both $Eu^{3+}$ and $UO_2^{2+}$, and the large enhancement of the $^5D_0 \rightarrow {}^7F_2$ transition of $Eu^{3+}$, also indicate strong surface complexation of $Eu^{3+}$ and $UO_2^{2+}$ on the gibbsite surface. Time-resolved luminescence spectra showed there are at least two distinct $UO_2^{2+}$ surface complexes formed on gibbsite. Here, we analyzed metal ion adsorption from the perspective of the surface OH groups for the first time and demonstrated that metal ion adsorption on gibbsite is likely to strongly impact its interfacial properties, including pH dependent surface charging and reactivity with respect to dissolution. This change to the interfacial properties will also influence particle aggregation and the subsequent rheological behavior of gibbsite suspensions. The technical approach demonstrated in this work and fundamental knowledge on the interfacial chemistry of solids and minerals will help with future design and synthesis of advanced materials for removal and recovery of toxic metal, *e.g.* chromium and uranium, from engineered systems.[94-96]

## Acknowledgments

The precision gibbsite nanomaterial synthesis, data interpretation, and manuscript development were supported by IDREAM (Interfacial Dynamics in Radioactive Environments and Materials), an Energy Frontier Research Center funded by the U.S. Department of Energy (DOE), Office of Science, Basic Energy Sciences (BES) (FWP 68932). Sample treatment, spectroscopy and microscopy analysis were supported by the Nuclear Process Initiative Laboratory Directed Research and Development at Pacific Northwest National Laboratory (PNNL). This research was performed at the William R. Wiley Environmental Molecular Science Laboratory (EMSL) at Pacific Northwest National Laboratory, a national scientific user facility sponsored by the U.S. DOE Office of Biological and Environmental Research. PNNL is operated by Battelle for the U.S. DOE under contract DE-AC05-76RLO 1830.

## Conflict of Interest

There is no conflict of interest.

## Supporting Information

Applicable.

## References

[1] J. Dejou, J. Guyot, C. Chaumont, H. Antoine, New observations on presence of gibbsite in areas of superficial decomposition and soils of crystalline and crystallophyllic massifs, *Annales agronomiques*, 1969, **20**, 639.

[2] A. D. Karathanasis, F. Adams, B. F. Hajek, Stability relationships in kaolinite, gibbsite, and Al-hydroxyinterlayered vermiculite soil systems, *Soil Science Society of America Journal*, 1983, **47**, 1247-1251, doi: 10.2136/sssaj1983.03615995004700060036x.

[3] J. A. McKeague, D. R. Grant, H. Kodama, G. J. Beke, C. Wang, Properties and genesis of a soil and the underlying gibbsite-bearing saprolite, Cape Breton Island, Canada, *Canadian Journal of Earth Sciences*, 1983, **20**, 37-48, doi: 10.1139/e83-004.

[4] C. R. Schefe, P. Kappen, L. Zuin, P. J. Pigram, C. Christensen, Addition of carboxylic acids modifies phosphate sorption on soil and boehmite surfaces: a solution chemistry and XANES spectroscopy study, *Journal of Colloid and Interface Science*, 2009, **330**, 51-59, doi: 10.1016/j.jcis.2008.10.044.

[5] W. Chesworth, The stability of gibbsite and boehmite at the surface of the earth, *Clays and Clay Minerals*, 1972, **20**, 369-374, doi: 10.1346/CCMN.1972.0200604.

[6] D. Panias, A. Krestou, Effect of synthesis parameters on precipitation of nanocrystalline boehmite from aluminate solutions, *Powder Technology*, 2007, **175**, 163-173, doi: 10.1016/j.powtec.2007.01.028.

[7] F. Granados-Correa, J. Jiménez-Becerril, Chromium (VI) adsorption on boehmite, *Journal of Hazardous Materials*, 2009, **162**, 1178-1184, doi: 10.1016/j.jhazmat.2008.06.002.

[8] P. J. Eng, T. P. Trainor, G. E. Brown Jr, G. A. Waychunas, M. Newville, S. R. Sutton, M. L. Rivers, Structure of the hydrated α-$Al_2O_3$ (0001) surface, *Science*, 2000, **288**, 1029-1033, doi: 10.1126/science.288.5468.1029.

[9] T. Kupcik, T. Rabung, J. Lützenkirchen, N. Finck, H. Geckeis, T. Fanghänel, Macroscopic and spectroscopic investigations on Eu(III) and Cm(III) sorption onto bayerite (β-$Al(OH)_3$) and corundum (α-$Al_2O_3$), *Journal of Colloid and Interface Science*, 2016, **461**, 215-224, doi: 10.1016/j.jcis.2015.09.020.

[10] E. Balan, M. Lazzeri, G. Morin, F. Mauri, First-principles study of the OH-stretching modes of gibbsite, *American Mineralogist*, 2006, **91**, 115-119, doi: 10.2138/am.2006.1922.

[11] J. D. Kubicki, S. E. Apitz, Molecular cluster models of aluminum oxide and aluminum hydroxide surfaces, *American Mineralogist*, 1998, **83**, 1054-1066, doi: 10.2138/am-1998-9-1014.

[12] D. L. Trimm, A. Stanislaus, The control of pore size in alumina catalyst supports: a review, *Applied Catalysis*, 1986, **21**, 215-238, doi: 10.1016/s0166-9834(00)81356-1.

[13] M. Trueba, S. P. Trasatti, γ-alumina as a support for catalysts: a review of fundamental aspects, *European Journal of Inorganic Chemistry*, 2005, **2005**, 3393-3403, doi: 10.1002/ejic.200500348.

[14] G. M. Thalib Basha, A. Srikanth, B. Venkateshwarlu, A critical review on nano structured coatings for alumina-titania (Al2O3-TiO2) deposited by air plasma spraying process (APS), *Materials Today: Proceedings*, 2020, **22**, 1554-1562, doi: 10.1016/j.matpr.2020.02.117.

[15] N. Huittinen, T. Rabung, J. Lützenkirchen, S. C. Mitchell, B.

R. Bickmore, J. Lehto, H. Geckeis, Sorption of Cm(III) and Gd(III) onto gibbsite, α-Al(OH)3: a batch and TRLFS study, *Journal of Colloid and Interface Science*, 2009, **332**, 158-164, doi: 10.1016/j.jcis.2008.12.017.

[16] S. Louaer, Y. Wang, L. Guo, Fast synthesis and size control of gibbsite nanoplatelets, their pseudomorphic dehydroxylation, and efficient dye adsorption, *ACS Applied Materials & Interfaces*, 2013, **5**, 9648-9655, doi: 10.1021/am402677v.

[17] S. N. Kerisit, Z. Shen, M. P. Prange, E. S. Ilton, Separation of radiolytic species at the boehmite-water interface, The *Journal of Physical Chemistry C*, 2019, **123**, 15534-15539, doi: 10.1021/acs.jpcc.9b02144.

[18] M. P. Prange, X. Zhang, M. E. Bowden, Z. Shen, E. S. Ilton, S. N. Kerisit, Predicting surface energies and particle morphologies of boehmite (γ-AlOOH) from density functional theory, *The Journal of Physical Chemistry C*, 2018, **122**, 10400-10412, doi: 10.1021/acs.jpcc.8b00278.

[19] M. P. Prange, X. Zhang, E. S. Ilton, L. Kovarik, M. H. Engelhard, S. N. Kerisit, Electronic response of aluminum-bearing minerals, *The Journal of Chemical Physics*, 2018, **149**, 024502, doi: 10.1063/1.5037104.

[20] Z. Shen, E. S. Ilton, M. P. Prange, C. J. Mundy, S. N. Kerisit, Diffusion mechanisms of radiolytic species in irradiated Al (oxy-) hydroxides, *The Journal of Physical Chemistry C*, 2018, **122**, 28990-28997, doi: 10.1021/acs.jpcc.8b07809.

[21] X. Zhang, P. L. Huestis, C. I. Pearce, J. Z. Hu, K. Page, L. M. Anovitz, A. B. Aleksandrov, M. P. Prange, S. Kerisit, M. E. Bowden, W. Cui, Z. Wang, N. R. Jaegers, T. R. Graham, M. Dembowski, H.-W. Wang, J. Liu, A. T. N'Diaye, M. Bleuel, D. F. R. Mildner, T. M. Orlando, G. A. Kimmel, J. A. La Verne, S. B. Clark, K. M. Rosso, Boehmite and gibbsite nanoplates for the synthesis of advanced alumina products, *ACS Applied Nano Materials*, 2018, **1**, 7115-7128, doi: 10.1021/acsanm.8b01969.

[22] S. T. Mergelsberg, M. Dembowski, M. E. Bowden, T. R. Graham, M. Prange, H.-W. Wang, X. Zhang, O. Qafoku, K. M. Rosso, C. I. Pearce, Cluster defects in gibbsite nanoplates grown at acidic to neutral pH, *Nanoscale*, 2021, **13**, 17373-17385, doi: 10.1039/d1nr01615f.

[23] W. D. Nesse, Introduction to Mineralogy, 2nd ed. Oxford University Press, Oxford, 2011.

[24] G. Sposito, The Environmental Chemistry of Aluminum, CRC Lewis Publishers, 2000.

[25] J. A. Davis, D. B. Kent, Surface complexation modeling in aqueous geochemistry, *Reviews in Mineralogy*, 1990 **23,** 177-260.

[26] R. A. Peterson, G. J. Lumetta, B. M. Rapko, A. P. Poloski, Modeling of boehmite leaching from actual Hanford high-level waste samples, *Separation Science and Technology*, 2007, **42**, 1719-1730, doi: 10.1080/01496390701242111.

[27] X. Zhang, W. Cui, J. Z. Hu, H.-W. Wang, M. P. Prange, C. Wan, N. R. Jaegers, M. Zong, H. Zhang, C. I. Pearce, P. Li, Z. Wang, S. B. Clark, K. M. Rosso, Transformation of gibbsite to boehmite in caustic aqueous solution at hydrothermal conditions, *Crystal Growth & Design*, 2019, **19**, 5557-5567, doi: 10.1021/acs.cgd.9b00468.

[28] J. S. Page, J. G. Reynolds, G. A. Cooke, B. E. Wells, Large cemented gibbsite agglomerates in alkaline nuclear waste at the Hanford site and the impacts to remediation, *Journal of Hazardous Materials*, 2020, **384**, 121318, doi: 10.1016/j.jhazmat.2019.121318.

[29] S. Chatterjee, M. A. Conroy, F. N. Smith, H.-J. Jung, Z. Wang, R. A. Peterson, A. Huq, D. G. Burtt, E. S. Ilton, E. C. Buck, Can Cr(iii) substitute for Al(iii) in the structure of boehmite? *RSC Advances*, 2016, **6**, 107628-107637, doi: 10.1039/c6ra20234a.

[30] W. Cui, X. Zhang, C. I. Pearce, M. H. Engelhard, H. Zhang, Y. Wang, S. M. Heald, S. Zheng, Y. Zhang, S. B. Clark, P. Li, Z. Wang, K. M. Rosso, Effect of Cr(III) adsorption on the dissolution of boehmite nanoparticles in caustic solution, *Environmental Science & Technology*, 2020, **54**, 6375-6384, doi: 10.1021/acs.est.9b07881.

[31] A. Hedin, O. Olsson, Crystalline rock as a repository for Swedish spent nuclear fuel, *Elements*, 2016, **12**, 247-252, doi: 10.2113/gselements.12.4.247.

[32] Y.-G. Chen, Z. Sun, W.-M. Ye, Y.-J. Cui, Adsorptive removal of Eu(III) from simulated groundwater by GMZ bentonite on the repository conditions, *Journal of Radioanalytical and Nuclear Chemistry*, 2017, **311**, 1839-1847, doi: 10.1007/s10967-017-5173-6.

[33] T. Missana, U. Alonso, A. M. Fernández, M. García-Gutiérrez, Colloidal properties of different smectite clays: significance for the bentonite barrier erosion and radionuclide transport in radioactive waste repositories, *Applied Geochemistry*, 2018, **97**, 157-166, doi: 10.1016/j.apgeochem.2018.08.008.

[34] T. Baumer, P. Kay, A. E. Hixon, Comparison of europium and neptunium adsorption to aluminum (hydr)oxide minerals, *Chemical Geology*, 2017, **464**, 84-90, doi: 10.1016/j.chemgeo.2017.02.006.

[35] S. Virtanen, F. Bok, A. Ikeda-Ohno, A. Rossberg, J. Lützenkirchen, T. Rabung, J. Lehto, N. Huittinen, The specific sorption of Np(V) on the corundum (α-$Al_2O_3$) surface in the presence of trivalent lanthanides Eu(III) and Gd(III): a batch sorption and XAS study, *Journal of Colloid and Interface Science*, 2016, **483**, 334-342, doi: 10.1016/j.jcis.2016.08.035.

[36] W. Cui, X. Zhang, C. I. Pearce, Y. Chen, S. Zhang, W. Liu, M. H. Engelhard, L. Kovarik, M. Zong, H. Zhang, E. D. Walter, Z. Zhu, S. M. Heald, M. P. Prange, J. J. De Yoreo, S. Zheng, Y. Zhang, S. B. Clark, P. Li, Z. Wang, K. M. Rosso, Cr(III) adsorption by cluster formation on boehmite nanoplates in highly alkaline solution, *Environmental Science & Technology*, 2019, **53**,

11043-11055, doi: 10.1021/acs.est.9b02693.

[37] N. Baumann, V. Brendler, T. Arnold, G. Geipel, G. Bernhard, Uranyl sorption onto gibbsite studied by time-resolved laser-induced fluorescence spectroscopy (TRLFS), *Journal of Colloid and Interface Science*, 2005, **290**, 318-324, doi: 10.1016/j.jcis.2004.10.076.

[38] Z. Wang, J. M. Zachara, W. Yantasee, P. L. Gassman, C. Liu, A. G. Joly, Cryogenic laser induced fluorescence characterization of U(VI) in Hanford vadose zone pore waters, *Environmental Science & Technology*, 2004, **38**, 5591-5597, doi: 10.1021/es049512u.

[39] H. Zhang, Y. Xie, Z. Tao, Sorption of uranyl ions on gibbsite: effects of contact time, pH, ionic strength, concentration and anion of electrolyte, *Colloids and Surfaces A: Physicochemical and Engineering Aspects*, 2005, **252**, 1-5, doi: 10.1016/j.colsurfa.2004.10.005.

[40] T. Hattori, T. Saito, K. Ishida, A. C. Scheinost, T. Tsuneda, S. Nagasaki, S. Tanaka, The structure of monomeric and dimeric uranyl adsorption complexes on gibbsite: a combined DFT and EXAFS study, *Geochimica et Cosmochimica Acta*, 2009, **73**, 5975-5988, doi: 10.1016/j.gca.2009.07.004.

[41] H.-S. Chang, G. V. Korshin, Z. Wang, J. M. Zachara, Adsorption of uranyl on gibbsite: a time-resolved laser-induced fluorescence spectroscopy study, *Environmental Science & Technology*, 2006, **40**, 1244-1249, doi: 10.1021/es051714i.

[42] E. Veilly, J. Roques, M.-C. Jodin-Caumon, B. Humbert, R. Drot, E. Simoni, Uranyl interaction with the hydrated (001) basal face of gibbsite: a combined theoretical and spectroscopic study, *The Journal of Chemical Physics*, 2008, **129**, 244704, doi: 10.1063/1.3042142.

[43] N. Baumann, V. Brendler, T. Arnold, G. Geipel, G. Bernhard, Uranyl sorption onto gibbsite studied by time-resolved laser-induced fluorescence spectroscopy (TRLFS), *Journal of Colloid and Interface Science*, 2005, **290**, 318-324, doi: 10.1016/j.jcis.2004.10.076.

[44] H. Wang, E. Borguet, E. C. Y. Yan, D. Zhang, J. Gutow, K. B. Eisenthal, Molecules at liquid and solid surfaces, *Langmuir*, 1998, **14**, 1472-1477, doi: 10.1021/la9707179.

[45] A. G. Lambert, P. B. Davies, D. J. Neivandt, Implementing the theory of sum frequency generation vibrational spectroscopy: a tutorial review, *Applied Spectroscopy Reviews*, 2005, **40**, 103-145, doi: 10.1081/ASR-200038326.

[46] H. C. Allen, E. A. Raymond, G. L. Richmond, Non-linear vibrational sum frequency spectroscopy of atmospherically relevant molecules at aqueous solution surfaces, *Current Opinion in Colloid & Interface Science*, 2000, **5**, 74-80, doi: 10.1016/s1359-0294(00)00033-9.

[47] H. Xu, D. Zhang, J. Hu, C. Tian, Y. R. Shen, Structure of the submonolayer of ethanol adsorption on a vapor/fused silica interface studied with sum frequency vibrational spectroscopy, *The Journal of Physical Chemistry A*, 2015, **119**, 4573-4580, doi: 10.1021/jp510706u.

[48] X. Zhang, W. Cui, K. L. Page, C. I. Pearce, M. E. Bowden, T. R. Graham, Z. Shen, P. Li, Z. Wang, S. Kerisit, A. T. N'Diaye, S. B. Clark, K. M. Rosso, Size and morphology controlled synthesis of boehmite nanoplates and crystal growth mechanisms, *Crystal Growth & Design*, 2018, **18**, 3596-3606, doi: 10.1021/acs.cgd.8b00394.

[49] X. Zhang, X. Zhang, T. R. Graham, C. I. Pearce, B. Layla Mehdi, A. T. N'Diaye, S. Kerisit, N. D. Browning, S. B. Clark, K. M. Rosso, Fast synthesis of gibbsite nanoplates and process optimization using box-behnken experimental design, *Crystal Growth & Design*, 2017, **17**, 6801-6808, doi: 10.1021/acs.cgd.7b01400.

[50] K. A. Link, C.-Y. Hsieh, A. Tuladhar, Z. Chase, Z. Wang, H. Wang, R. A. Walker, Vibrational studies of saccharide-induced lipid film reorganization at aqueous/air interfaces, *Chemical Physics*, 2018, **512**, 104-110, doi: 10.1016/j.chemphys.2018.02.011.

[51] L. Zhang, L. Yan, Z. Wang, D. D. Laskar, M. S. Swita, J. R. Cort, B. Yang, Characterization of lignin derived from water-only and dilute acid flowthrough pretreatment of poplar wood at elevated temperatures, *Biotechnology for Biofuels*, 2015, **8**, 1-14, doi: 10.1186/s13068-015-0377-x.

[52] A. Tuladhar, Z. A. Chase, M. D. Baer, B. A. Legg, J. Tao, S. Zhang, A. D. Winkelman, Z. Wang, C. J. Mundy, J. J. De Yoreo, H.-F. Wang, Direct observation of the orientational anisotropy of buried hydroxyl groups inside muscovite mica, *Journal of the American Chemical Society*, 2019, **141**, 2135-2142, doi: 10.1021/jacs.8b12483.

[53] Z. Wang, A. R. Felmy, Y. Xia, E. C. Buck, Observation of aqueous Cm(III)/Eu(III) and $UO2^{2+}$ nanoparticulates at concentrations approaching solubility limit by laser-induced fluorescence spectroscopy, *Journal of Alloys and Compounds*, 2006, **418**, 166-170, doi: 10.1016/j.jallcom.2005.07.080.

[54] Z. Wang, J. M. Zachara, J.-F. Boily, Y. Xia, T. C. Resch, D. A. Moore, C. Liu, Determining individual mineral contributions to U(VI) adsorption in a contaminated aquifer sediment: a fluorescence spectroscopy study, *Geochimica et Cosmochimica Acta*, 2011, **75**, 2965-2979, doi: 10.1016/j.gca.2011.03.008.

[55] Y. Liu, D. Ma, R. A. Blackley, W. Zhou, X. Han, X. Bao, Synthesis and characterization of gibbsite nanostructures, *The Journal of Physical Chemistry C*, 2008, **112**, 4124-4128, doi: 10.1021/jp7101572.

[56] Z. Wang, E. D. Walter, M. Sassi, X. Zhang, H. Zhang, X. S. Li, Y. Chen, W. Cui, A. Tuladhar, Z. Chase, A. D. Winkelman, H.-F. Wang, C. I. Pearce, S. B. Clark, K. M. Rosso, The role of surface hydroxyls on the radiolysis of gibbsite and boehmite

nanoplatelets, *Journal of Hazardous Materials*, 2020, **398**, 122853, doi: 10.1016/j.jhazmat.2020.122853.

[57] M. Sassi, Z. Wang, E. D. Walter, X. Zhang, H. Zhang, X. S. Li, A. Tuladhar, M. Bowden, H.-F. Wang, S. B. Clark, K. M. Rosso, Surface hydration and hydroxyl configurations of gibbsite and boehmite nanoplates, *The Journal of Physical Chemistry C*, 2020, **124**, 5275-5285, doi: 10.1021/acs.jpcc.0c00659.

[58] J. T. Huneke, R. E. Cramer, R. Alvarez, S. A. El-Swaify, The identification of gibbsite and bayerite by laser Raman spectroscopy, *Soil Science Society of America Journal*, 1980, **44**, 131-134, doi: 10.2136/sssaj1980.03615995004400010027x.

[59] S.-L. Wang, C. T. Johnston, Assignment of the structural OH stretching bands of gibbsite, *American Mineralogist*, 2000, **85**, 739-744, doi: 10.2138/am-2000-5-612.

[60] J. D. Russell, R. L. Parfitt, A. R. Fraser, V. C. Farmer, Surface structures of gibbsite goethite and phosphated goethite, *Nature*, 1974, **248**, 220-221, doi: 10.1038/248220a0.

[61] R. Guillaumont, F. J. Mompean, Update on the chemical thermodynamics of uranium, neptunium, plutonium, americium and technetium, Elsevier: Amsterdam, 2003, **5**, 64-70.

[62] J. Nonkumwong, U. J. Erasquin, K. W. Sy Piecco, U. I. Premadasa, A. M. Aboelenen, A. Tangonan, J. Chen, D. Ingram, L. Srisombat, K. Leslee Asetre Cimatu, Successive surface reactions on hydrophilic silica for modified magnetic nanoparticle attachment probed by sum-frequency generation spectroscopy, *Langmuir*, 2018, **34**, 12680-12693, doi: 10.1021/acs.langmuir.8b01333.

[63] A. Tuladhar, S. Dewan, J. D. Kubicki, E. Borguet, Spectroscopy and ultrafast vibrational dynamics of strongly hydrogen bonded OH species at the $\alpha$-$Al_2O_3(11\bar{2}0)/H_2O$ interface, *The Journal of Physical Chemistry C*, 2016, **120**, 16153-16161, doi: 10.1021/acs.jpcc.5b12486.

[64] G. Rupprechter, Surface vibrational spectroscopy from ultrahigh vacuum to atmospheric pressure: adsorption and reactions on single crystals and nanoparticle model catalysts monitored by sum frequency generation spectroscopy, *Physical Chemistry Chemical Physics*, 2001, **3**, 4621-4632, doi: 10.1039/b104354b.

[65] H. Ishida, K. Iwatsu, J. Kubota, A. Wada, K. Domen, C. Hirose, in situ SFG spectroscopy of film growth. II. Deposition of formic acid on Ni(110) surface, *The Journal of Chemical Physics*, 1998, **108**, 5957-5964, doi: 10.1063/1.476007.

[66] D. Simonelli, M. J. Shultz, Sum frequency generation orientation analysis of molecular ammonia on the surface of concentrated solutions, *The Journal of Chemical Physics*, 2000, **112**, 6804-6816, doi: 10.1063/1.481255.

[67] L. Velarde, Z. Lu, H.-F. Wang, Coherent vibrational dynamics and high-resolution nonlinear spectroscopy: a comparison with the air/DMSO liquid interface, *Chinese Journal of Chemical Physics*, 2013, **26**, 710-720, doi: 10.1063/1674-0068/26/06/710-720.

[68] R. J. Fellows, Z. Wang, C. C. Ainsworth, Europium uptake and partitioning in oat (avena sativa) roots as studied by laser-induced fluorescence spectroscopy and confocal microscopy profiling technique, *Environmental Science & Technology*, 2003, **37**, 5247-5253, doi: 10.1021/es0343609.

[69] W. D. Horrocks Jr, D. R. Sudnick, Lanthanide ion luminescence probes of the structure of biological macromolecules, *Accounts of Chemical Research*, 1981, **14**, 384-392, doi: 10.1021/ar00072a004.

[70] W. DeW Horrocks Jr, D. R. Sudnick, Lanthanide ion probes of structure in biology. Laser-induced luminescence decay constants provide a direct measure of the number of metal-coordinated water molecules, *Journal of the American Chemical Society*, 1979, **101**, 334-340, doi: 10.1021/ja00496a010.

[71] Z. Wang, J. M. Zachara, P. L. Gassman, C. Liu, O. Qafoku, W. Yantasee, J. G. Catalano, Fluorescence spectroscopy of U(VI)-silicates and U(VI)-contaminated Hanford sediment, *Geochimica et Cosmochimica Acta*, 2005, **69**, 1391-1403, doi: 10.1016/j.gca.2004.08.028.

[72] Z. Wang, A. R. Felmy, Y. Xia, E. C. Buck, Observation of aqueous Cm(III)/Eu(III) and $UO2^{2+}$ nanoparticulates at concentrations approaching solubility limit by laser-induced fluorescence spectroscopy, *Journal of Alloys and Compounds*, 2006, **418**, 166-170, doi: 10.1016/j.jallcom.2005.07.080.

[73] H. Geckeis, J. Lützenkirchen, R. Polly, T. Rabung, M. Schmidt, Mineral-water interface reactions of actinides, *Chemical Reviews*, 2013, **113**, 1016-1062, doi: 10.1021/cr300370h.

[74] H. Pieper, D. Bosbach, P. J. Panak, T. Rabung, T. Fanghänel, Eu(III) coprecipitation with the trioctahedral clay mineral, hectorite, *Clays and Clay Minerals*, 2006, **54**, 45-53, doi: 10.1346/CCMN.2006.0540106.

[75] W. Dew Horrocks Jr, M. Albin, Lanthanide ion luminescence in coordination chemistry and biochemistry, Progress in Inorganic Chemistry. Hoboken, NJ, USA: John Wiley & Sons, Inc., 2007, 1-104, doi: 10.1002/9780470166321.ch1.

[76] F. S. Richardson, Terbium(III) and europium(III) ions as luminescent probes and stains for biomolecular systems, *Chemical Reviews*, 1982, **82**, 541-552, doi: 10.1021/cr00051a004.

[77] F. S. Richardson, M. F. Reid, J. J. Dallara, R. D. Smith, Energy levels of lanthanide ions in the cubic Cs2NaLnCl6 and Cs2NaYCl6: Ln3+ (doped) systems, *The Journal of Chemical Physics*, 1985, **83**, 3813-3830, doi: 10.1063/1.449092.

[78] R. Arppe-Tabbara, M. R. Carro-Temboury, C. Hempel, T. Vosch, T. J. Sørensen, Frontispiece: luminescence from lanthanide(III) ions bound to the glycocalyx of Chinese hamster ovary cells, *Chemistry - A European Journal*, 2018, **24**, 11885-

11889, doi: 10.1002/chem.201884667.

[79] S. H. Hewitt, S. J. Butler, Application of lanthanide luminescence in probing enzyme activity, *Chemical Communications*, 2018, **54**, 6635-6647, doi: 10.1039/c8cc02824a.

[80] Ting, Chen, Single-chain lanthanide luminescence biosensors for cell-based imaging and screening of protein-protein interactions, *iScience*, 2020, **23**, 101533, doi: 10.1016/j.isci.2020.101533.

[81] X. Liu, B. Li, Y. Xu, Z. Li, Y. Zhang, Z.-J. Ding, H. Cui, J. Wang, H.-B. Hou, H. Li, A highly selective lanthanide-containing probe for ratiometric luminescence detection of an anthrax biomarker, *Dalton Transactions*, 2019, **48**, 7714-7719, doi: 10.1039/c9dt01477b.

[82] E. Balboni, J. M. Morrison, Z. Wang, M. H. Engelhard, P. C. Burns, Incorporation of Np(V) and U(VI) in carbonate and sulfate minerals crystallized from aqueous solution, *Geochimica et Cosmochimica Acta*, 2015, **151**, 133-149, doi: 10.1016/j.gca.2014.10.027.

[83] E. J. Elzinga, C. D. Tait, R. J. Reeder, K. D. Rector, R. J. Donohoe, D. E. Morris, Spectroscopic investigation of U(VI) sorption at the calcite-water interface, *Geochimica et Cosmochimica Acta*, 2004, **68**, 2437-2448, doi: 10.1016/j.gca.2003.09.023.

[84] D. E. Morris, P. G. Allen, J. M. Berg, C. J. Chisholm-Brause, S. D. Conradson, R. J. Donohoe, N. J. Hess, J. A. Musgrave, C. D. Tait, Speciation of uranium in fernald soils by molecular spectroscopic methods: characterization of untreated soils, *Environmental Science & Technology*, 1996, **30**, 2322-2331, doi: 10.1021/es950745i.

[85] P. P. Barthelemy, G. R. Choppin, Luminescence study of complexation of europium and dicarboxylic acids, *Inorganic Chemistry*, 1989, **28**, 3354-3357, doi: 10.1021/ic00316a023.

[86] T. Ozaki, M. Arisaka, T. Kimura, A. Francis, Z. Yoshida, Empirical method for prediction of the coordination environment of Eu(III) by time-resolved laser-induced fluorescence spectroscopy, *Analytical and Bioanalytical Chemistry*, 2002, **374**, 1101-1104, doi: 10.1007/s00216-002-1587-1.

[87] Z.-M. Wang, L. J. van de Burgt, G. R. Choppin, Spectroscopic study of lanthanide(III) complexes with carboxylic acids, *Inorganica Chimica Acta*, 1999, **293**, 167-177, doi: 10.1016/s0020-1693(99)00234-0.

[88] Yoshio, Takahashi, Direct observation of Cm(III)-fulvate species on fulvic acid-montmorillonite hybrid by laser-induced fluorescence spectroscopy, *Geochimica et Cosmochimica Acta*, 2002, **66**, 1-12, doi: 10.1016/S0016-7037(01)00748-7.

[89] G. Blasse, Luminescence of inorganic solids: from isolated centres to concentrated systems, *Progress in Solid State Chemistry*, 1988, **18**, 79-171, doi: 10.1016/0079-6786(88)90004-0.

[90] K. Grossmann, T. Arnold, A. Ikeda-Ohno, R. Steudtner, G. Geipel, G. Bernhard, Fluorescence properties of a uranyl(V)-carbonate species[U(V)O2(CO3)3]5–at low temperature, *Spectrochimica Acta Part A: Molecular and Biomolecular Spectroscopy*, 2009, **72**, 449-453, doi: 10.1016/j.saa.2008.10.041.

[91] A. Günther, G. Geipel, G. Bernhard, Complex formation of U(VI) with the amino acid L-threonine and the corresponding phosphate ester O-phospho-L-threonine, *Radiochimica Acta*, 2006, **94**, 845-851, doi: 10.1524/ract.2006.94.12.845.

[92] S. Sachs, V. Brendler, G. Geipel, Uranium(VI) complexation by humic acid under neutral pH conditions studied by laser-induced fluorescence spectroscopy, *Radiochimica Acta*, 2007, **95**, 103-110, doi: 10.1524/ract.2007.95.2.103.

[93] Z. Wang, J. M. Zachara, C. Liu, P. L. Gassman, A. R. Felmy, S. B. Clark, A cryogenic fluorescence spectroscopic study of uranyl carbonate, phosphate and oxyhydroxide minerals, *Radiochimica Acta*, 2008, **96**, 591-598, doi: 10.1524/ract.2008.1541.

[94] L. Yao, Z. Shen, Z. Ji, Y. Hu, D. Tang, G. Zhao, X. Wang, Cr(VI) detoxification and simultaneous selective recovery of Cr resource from wastewater via photo-chemical extraction using biomass, *Science Bulletin*, 2022, **67**, 2154-2157, doi: 10.1016/j.scib.2022.10.013.

[95] L. Yao, Y. Hu, Y. Zou, Z. Ji, S. Hu, C. Wang, P. Zhang, H. Yang, Z. Shen, D. Tang, S. Zhang, G. Zhao, X. Wang, Selective and efficient photoextraction of aqueous Cr(VI) as a solid-state polyhydroxy Cr(V) complex for environmental remediation and resource recovery, *Environmental Science & Technology*, 2022, **56**, 14030-14037, doi: 10.1021/acs.est.2c03994.

[96] H. Zhang, P. Li, Z. Wang, W. W. Cui, Y. Zhang, Y. Zhang, S. Zheng, Y. Zhang, Sustainable disposal of Cr(VI): adsorption-reduction strategy for treating textile wastewaters with amino-functionalized boehmite hazardous solid wastes, *ACS Sustainable Chemistry & Engineering*, 2018, **6**, 6811-6819, doi: 10.1021/acssuschemeng.8b00640.